Downloaded from UvA-DARE, the institutional repository of the University of Amsterdam (UvA)
http://hdl.handle.net/11245/2.37162

File ID uvapub:37162
Filename 162119y.pdf
Version unknown

SOURCE (OR PART OF THE FOLLOWING SOURCE):
Type article
Title The peculiar circumstellar environment of NGC 2024 IRS2
Author(s) A. Lenorzer, A. Bik, A. de Koter, S.E. Kurtz, L.B.F.M. Waters, L. Kaper, C.E. Jones, T.R. Geballe
Faculty FNWI: Astronomical Institute Anton Pannekoek (IAP)
Year 2004

FULL BIBLIOGRAPHIC DETAILS:
http://hdl.handle.net/11245/1.228273

Copyright

It is not permitted to download or to forward/distribute the text or part of it without the consent of the author(s) and/or copyright holder(s), other than for strictly personal, individual use, unless the work is under an open content licence (like Creative Commons).

UvA-DARE is a service provided by the library of the University of Amsterdam (http://dare.uva.nl)
(pagedate: 2014-11-16)

A&A 414, 245–259 (2004)
DOI: 10.1051/0004-6361:20031580
© ESO 2004

Astronomy & Astrophysics

The peculiar circumstellar environment of NGC 2024 IRS2

A. Lenorzer[1], A. Bik[1], A. de Koter[1], S. E. Kurtz[2], L. B. F. M. Waters[1,3], L. Kaper[1], C. E. Jones[4], and T. R. Geballe[5]

[1] Astronomical Institute "Anton Pannekoek", Kruislaan 403, 1098 SJ Amsterdam, The Netherlands
[2] Instituto de Astronomía, Universidad Nacional Autónoma de México, Apdo. Postal 3-72, 58090 Morelia, Mich. México
[3] Instituut voor Sterrenkunde, K.U. Leuven, Celestijnenlaan 200B, 3001 Heverlee, Belgium
[4] Department of Physics and Astronomy, The University of Western Ontario, London, Ontario, Canada N6A 3K7 Gemini Observatory, 670 N. A'ohoku Place, Hilo, HI 96720, USA

Received 20 March 2003 / Accepted 2 October 2003

Abstract. We re-examine the nature of NGC 2024 IRS2 in light of the recent discovery of the late O-type star, IRS2b, located 5″ from IRS2. Using L-band spectroscopy, we set a lower limit of A_V = 27.0 mag on the visual extinction towards IRS2. Arguments based on the nature of the circumstellar material, favor an A_V of 31.5 mag. IRS2 is associated with the UCHII region G206.543–16.347 and the infrared source IRAS 05393–0156. We show that much of the mid-infrared emission towards IRS2, as well as the far infrared emission peaking at ∼100 μm, do not originate in the direct surroundings of IRS2, but instead from an extended molecular cloud. Using new K-, L- and L'-band spectroscopy and a comprehensive set of infrared and radio continuum measurements from the literature, we apply diagnostics based on the radio slope, the strength of the infrared hydrogen recombination lines, and the presence of CO band-heads to constrain the nature and spatial distribution of the circumstellar material of IRS2. Using simple gaseous and/or dust models of prescribed geometry, we find strong indications that the infrared flux originating in the circumstellar material of IRS2 is dominated by emission from a dense gaseous disk with a radius of about 0.6 AU. At radio wavelengths the flux density distribution is best described by a stellar wind recombining at a radius of about 100 AU. Although NGC 2024 IRS2 shares many similarities with BN-like objects, we do not find evidence for the presence of a dust shell surrounding this object. Therefore, IRS2 is likely more evolved.

Key words. stars: circumstellar matter – early-type – individual: NGC 2024 IRS2 – infrared: stars

1. Introduction

NGC 2024 is one of the four major nebulae in the nearby giant star forming complex Orion B. Located at about 363 pc (Brown et al. 1994) this nearby H II region is particularly active in star formation and has therefore been extensively studied at many wavelengths. The optical image of NGC 2024 (the Flame Nebula) shows a bright nebulosity with a central elongated obscuration in the north-south direction. The heavy extinction renders most of the nebula unobservable, from the UV to about one micron.

The ionizing source of NGC 2024 was unknown until very recently (Bik et al. 2003), although numerous secondary indicators suggested that the dominant source must be a late-O main-sequence star (e.g. Cesarsky 1977). The ionizing star was searched for in the near-infrared where it was expected to be the brightest source in NGC 2024. This led to the discovery of IRS2 by Grasdalen (1974). IRS2 has been extensively studied in the near-infrared (Jiang et al. 1984; Black & Willner 1984; Chalabaev & Léna 1986; Barnes et al. 1989; Nisini et al. 1994), although it was eventually recognized that it is incapable of powering the H II region (e.g., Nisini et al. 1994). NGC 2024 hosts the strong IRAS source 05393–0156 whose colors fulfill the criteria of Ultra-Compact H II (UCHII) regions as defined by Wood & Churchwell (1989). Kurtz et al. (1994) and Walsh et al. (1998) identified the compact radio source G206.543–16.347, 72.8″ from the IRAS source, but coincident with IRS2.

The dominant ionizing source of NGC 2024 has recently been identified as IRS2b. IRS2 is only 5″ away from IRS2b, for which an extinction has been reliably determined (Bik et al. 2003). We address the nature of the circumstellar material of IRS2 in light of this discovery. If IRS2 is not the dominant source of ionization of NGC 2024, what makes it so bright at infrared wavelengths? Is the star surrounded by a dust shell and/or a circumstellar disk? Is IRS2 a massive young stellar object, and if so, do we observe remnants from the star formation process?

In this study, we make use of spectroscopic observations obtained with The *Very Large Telescope* (VLT) and the *United Kingdom Infrared Telescope* (UKIRT) and photometric measurements from the literature. The paper is organized as follows: in Sect. 2 we describe the new spectroscopic

Send offprint requests to: A. Lenorzer,
e-mail: lenorzer@science.uva.nl

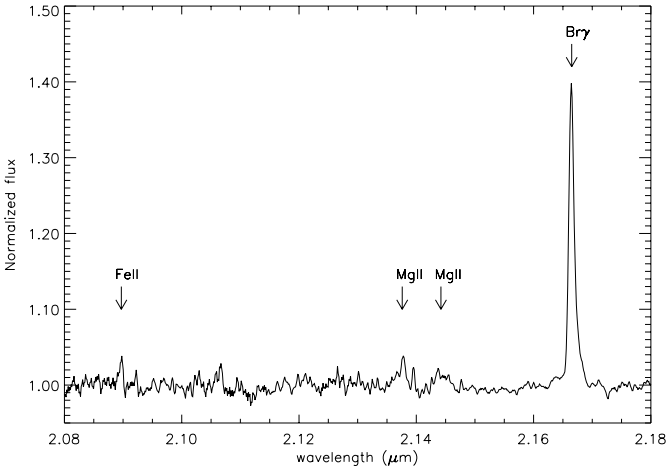

Fig. 1. 2.08−2.18 μm spectrum of NGC 2024 IRS2 obtained with ISAAC/VLT at $R \simeq 8000$. Line identifications and properties are given in Table 1.

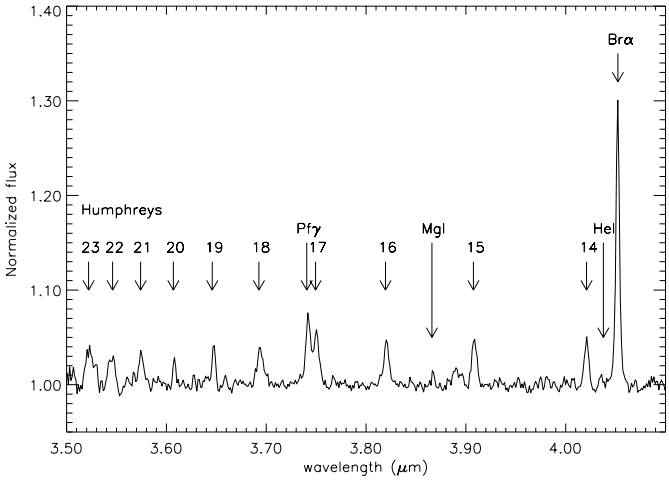

Fig. 2. 3.5−4.1 μm spectrum of NGC 2024 IRS2 obtained with CGS4/UKIRT at a resolving power of $R \sim 1500$. Line identifications and properties are given in Table 1.

observations. We present the flux density distribution in Sect. 3 and propose a set of diagnostics to investigate the circumstellar material of IRS2 in Sect. 4. We employ and discuss the merits of three simple models to fit the observations in Sect. 5. We summarize our findings in Sect. 6.

2. Observations

2.1. Observations and data reduction

A 2.08−2.18 μm spectrum of IRS2, with a spectral resolving power $R \simeq 8000$ and signal-to-noise ratio $S/N \sim 130$, was obtained using the Infrared Spectrometer And Array Camera (ISAAC) at the VLT on March 20, 2000. The spectrum was reduced using standard procedures. Telluric absorption lines were removed using the A2 V star HD 39908 observed under identical sky conditions as IRS2. Over the wavelength range of the Brγ line, we substituted a spectrum of telluric features in place of the standard spectrum, instead of interpolating across the Brγ line of the standard star as is usually done. As we are interested in the broad features in the line profile in IRS2, we prefer to have easily recognizable residuals from narrow telluric lines rather than broad residuals from the inaccurate removal of the broad Brγ line of the standard star.

L-band spectra of both IRS2 and IRS2b were obtained using ISAAC on February 22, 2002, with a resolving power $R \simeq 1200$. The response function was derived by dividing the spectrum of an A6 II star (HD 73634), observed under similar conditions, by a synthetic spectrum compiled from a MARCS model atmosphere with parameters $T_{\rm eff} = 8100$ K, $\log g = 2.76$, and [Fe/H] = 0.00 (Decin, priv. comm.). The model assumes plane-parallel layers and solar abundances. For the synthetic spectrum calculations the atomic line list of Sauval (Decin 2000) and the H-line list of Kurucz (1991) were used. For more details about the atmosphere models, see Decin et al. (2000) and Plez et al. (1992).

The L'-band (3.5−4.1 μm) spectrum was obtained on December 23, 2000 (UT), using the Cooled Grating Spectrometer 4 (CGS4; Mountain et al. 1990) on UKIRT. CGS4's 40 l/mm grating was used in first order with the 300 mm focal length camera and the 0.6″ wide slit, giving a nominal resolving power $R \sim 1500$. The array was stepped to provide two data points per resolution element. A signal-to-noise ratio of ∼100 was achieved on the continuum. We used the Starlink Figaro package for data reduction. Wavelength calibration was done using the second order spectrum of an argon arc lamp. The spectrum was reduced using the F0 V standard BS 1474 and the spectrum of a star of the same spectral type observed at similar spectral resolution with the Short Wavelength Spectrometer (SWS, de Graauw et al. 1996) on the *Infrared Space Observatory* (ISO, Kessler et al. 1996). We built a responsivity curve by dividing the L'-band spectrum of the standard star by the ISO spectrum of this F0 V star and used it to reduce the spectrum of IRS2.

2.2. Line properties and identifications

The 2.08−2.18 μm and 3.5−4.1 μm spectra of IRS2 are presented in Figs. 1 and 2. The spectra only include emission lines, mainly from hydrogen. We identified two lines of Mg II and possibly one line of Fe II at λ2.089 μm, one line of Mg I at λ3.866 μm and one line of He I at λ4.038 μm. The Mg II and Fe II lines indicate the presence of very high density and fairly cool gas close to the star (e.g. Hamann & Simon 1987). The 2.08−2.18 μm spectrum of IRS2 is similar to the spectra of Group 3 Be stars as proposed by Clark & Steele (2000), having spectral types in the range B1–B4. That group contains five stars all showing Mg II and Brγ in emission and no He I; four of them also show Fe II in emission. The He I 2.06 μm line, usually the strongest line in the *K*-band, is not covered in our spectrum, but is not present in the *K*-band spectrum of IRS2 obtained by Thompson et al. (1981). The equivalent width (*EW*)

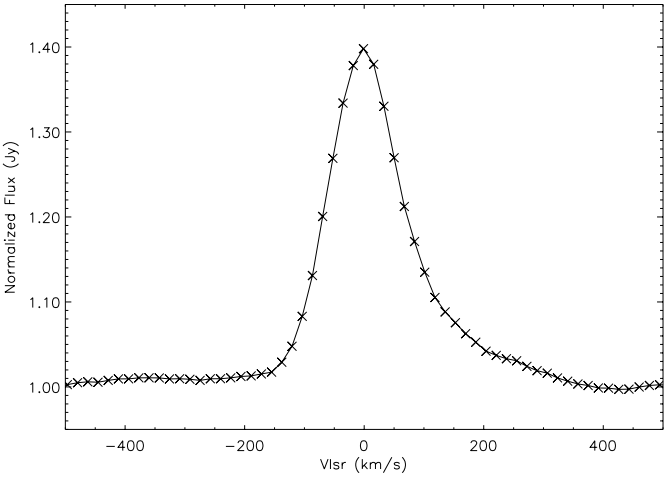

Fig. 3. The 2.17 μm Brγ line of IRS2 obtained with VLT/ISAAC. The line peaks at $v_{\rm lsr}$ = 0 km s^{-1}and has a wing extending ~400 km s^{-1} to the red side of the profile.

of the Brγ line is larger than 8 Å in all Group 3 stars, but is somewhat less in IRS2 (5.3 ± 0.1 Å).

The Mg II, Pfγ and Humphreys series lines are fairly broad with full widths at half maximum (*FWHM*s) of about 400 km s^{-1}. The Brackett lines are much narrower, with deconvolved *FWHM*s of 145 km s^{-1} for Brγ and 200 km s^{-1} for Brα. The values in Table 1 are not deconvolved by the instrumental profile, but deconvolution has only a small effect except for Brα. The difference in *FWHM* between the Brackett and other hydrogen lines is investigated further in Sect.4.2.

Previous near-infrared spectroscopic observations of recombination lines in NGC 2024 IRS2 have been reported by Thompson et al. (1981), Smith et al. (1984), Chalabaev & Léna (1986), Geballe et al. (1987), Maihara et al. (1990), and Nisini et al. (1994). Both the line fluxes and line profiles have shown significant variations. Only small variations in the line fluxes were observed between 1980 and 1989. In 1991, however, the line fluxes increase greatly (up to 10 times for Brα; Nisini et al. 1994). The proportional increase was larger for Brα than for Brγ and Pfγ. The increase was followed by a decrease during the period 1992–1994. There have been no reported measurements of these lines since 1994.

High-resolution spectroscopy (R ~ 10 000) by Smith et al. (1984) and Chalabaev & Léna (1986) showed that the peaks of the Brα, Pfγ, and Brγ lines were at velocities in the range 20 < $v_{\rm lsr}$ < 50 km s^{-1} and that the lines had extended blue-shifted wings. In 1992 all three lines peaked at $v_{\rm lsr}$ = −25 km s^{-1} and had extended red-shifted wings (Nisini et al. 1994). Our 2000 spectrum shows the peak of Brγ near $v_{\rm lsr}$ = 0 km s^{-1} and a very extended wing on the red side of the profile (see Fig. 3). The widths of the lines, both at half maximum and at zero intensity (*FWZI*), are comparable in 1984, 1992 and 1993 and are about 100 and 250 km s^{-1}, respectively. However, in 2000 all three lines had much larger widths. The measured *FWZI* of ~600 km s^{-1} for the Brγ line is much larger than has previously been seen in any of the lines. The large width is mainly due to the red wing.

Both the ISAAC and UKIRT measurements are in smaller apertures than all previous observations. The narrower profiles measured by Smith et al. (1984), Chalabaev & Léna (1986) and Nisini et al. (1994) might result from a larger contribution from extended gas with lower velocity dispersion. Our new high-resolution observations demonstrate that eight years after the outburst the lines have not returned to their pre-outburst width, shape, and peak velocity. Therefore we question if $v_{\rm lsr}$ = 40 km s^{-1} is the actual systemic velocity for IRS2. We note that the extended molecular cloud of NGC 2024 has $v_{\rm lsr}$ of 6 km s^{-1} in the region surrounding our program star (Krügel et al. 1982). IRS2 likely has a similar velocity. We do not pursue on the nature of the observed line variability as this requires consecutive observations on timescales much shorter than are available. This variability was already pointed out by Nisini et al. (1994), who also suggest several explanations for the line behaviour between 1981 and 1994.

3. The spectral energy distribution

In Fig. 4 we display the spectral energy distribution (SED) of IRS2 from the near-infrared to the radio domain. The SED is based on photometric data compiled from the literature plus spectra obtained using the SWS and LWS instruments on ISO. The interpretation of the plotted data is not straightforward, as measurements have been obtained with widely different apertures. We provide information on all data points in the figure, including beam sizes, measured magnitudes and fluxes, as well as the observational technique (when non-photometric) in Tables 2–4 in the appendix.

3.1. Contribution of IRS2 to the observed spectral energy distribution

Variations between different observations at the same wavelength can be noticed, the most striking being in the range of 3 to 30 μm. It is crucial to determine the dominant cause of these variations in order to measure the flux directly attributable to IRS2. The variations could be due to intrinsic variability of IRS2, to the extended background, or to other discrete sources. The region surrounding IRS2 is far from empty at infrared wavelengths (cf. Bik et al. 2003) and we thus expect some dependence of the observed flux on aperture size. In the following we separately discuss four wavelength ranges: the near-infrared (1−10 μm), the mid-infrared (10−25 μm), the far-infrared to sub-millimeter (25 μm−0.2 cm) and the radio domain (0.2−6 cm).

Most of the near-infrared observations were made with beam sizes less than or equal to 15″; only the data observed by Frey et al. (1979) were obtained through a larger aperture (63″). The aperture used by Grasdalen (1974) is not specified, however the bolometer systems they used on the 1.3m and 2.1m telescopes at Kitt Peak had aperture diameters less than 12″ (Joyce, priv. comm.), the ones they used likely being smaller than 8.5″ (Rieke, priv. comm.). The fluxes observed through apertures less than or equal to 20″

Table 1. Wavelength, emission line equivalent width, full width at half maximum, and identification of the lines present in the 2.08−2.18 μm and the 3.5−4.1 μm spectra. The last columns list the spectral resolving power and beam size. Lines for which no measured quantities are given represent uncertain identifications.

λ (μm)	*EW* (Å)	*FWHM* (km s^{-1})	Identification	*R*	beam ($''$)
2.090	0.30 ± 0.06	117	Fe II ($3d^6 4p$–$3d^6 4s$)	8000	0.6 × 0.9
2.138	0.6 ± 0.1	290	Mg II (5s–5p)	8000	0.6 × 0.9
2.144	0.4 ± 0.1	320	Mg II (5s–5p)	8000	0.6 × 0.9
2.166	5.3 ± 0.1	150	H I (4–7)	8000	0.6 × 0.9
3.575	1.7 ± 0.3	389	H I (6–21)	1500	0.6 × 1.8
3.608	1.3 ± 0.3	289	H I (6–20)	1500	0.6 × 1.8
3.647	2.0 ± 0.3	337	H I (6–19)	1500	0.6 × 1.8
3.694	2.3 ± 0.3	393	H I (6–18)	1500	0.6 × 1.8
3.742	5.0 ± 0.3	470	H I (5–8)	1500	0.6 × 1.8
3.750	3.0 ± 0.3	470	H I (6–17)	1500	0.6 × 1.8
3.820	2.9 ± 0.3	460	H I (6–16)	1500	0.6 × 1.8
3.866	≤0.3		Mg I (3s.4f–3s.5g)	1500	0.6 × 1.8
3.908	3.3 ± 0.3	470	H I (6–15)	1500	0.6 × 1.8
4.021	3.5 ± 0.3	440	H I (6–14)	1500	0.6 × 1.8
4.038	≤0.3		He I (1s.4d–1s.5f)	1500	0.6 × 1.8
4.052	14.5 ± 0.2	290	H I (4–5)	1500	0.6 × 1.8

(including the ISO/SWS spectrum) do not show any trend with aperture size. The higher values obtained by Nisini et al. (1994), which were observed with simultaneous line enhancement and shift, most likely originate from variations close to or in IRS2. The *J*-band measurement of Grasdalen (1974) is brighter than other observations by 0.8 mag. It is difficult to attribute this value to source variability as it is the only band affected by this discrepancy. We conclude that IRS2 is the dominant source in the 1−10 μm region through aperture diameters less than or equal to 20$''$.

The mid-infrared SED consists of four data sets. Grasdalen (1974) and Walsh et al. (2001) observed similar fluxes at ∼10 μm through small apertures. The ISO/SWS flux is higher than the other mid-IR values suggesting that IRS2 is not the dominant source in the mid-infrared within the 14 × 20$''$ ISO beam. The IRAS fluxes are 20 and 600 times larger than the ones of Grasdalen (1974) at 12 and 25 μm respectively, and are obtained through much larger apertures. Moreover, there is a large offset of 72.8$''$ between the position of IRS2 and IRAS 05393–0156; this IRAS point source has commonly been associated with IRS2 (e.g. Kurtz et al. 1994 or Walsh et al. 1998), but is actually closer to FIR5 (Mezger et al. 1988), supporting the view that IRS2 is not the dominant source in the IRAS beam.

The IRS2 region has not been observed at far-infrared to sub-millimeter wavelengths with aperture sizes smaller than 40$''$. ISO/LWS observed three different sources between 43 and 197 μm within NGC 2024: IRS2, FIR3 and FIR5. The beams including IRS2 and FIR3 overlap by about 50% whereas the beam of FIR5 has only a very small fraction in common with the others. The three spectra are very similar suggesting that at these wavelengths the emission is coming from the extended surroundings and not from individual sources (see Giannini et al. 2000).

In the radio domain we only consider data obtained with interferometers, i.e. with small beam sizes. After inspection of the original data, we feel that the 6 cm data point of Snell & Bally (1986; 2.8 mJy) is too low and that the 1.3 cm point (Gaume et al. 1992; 19 mJy) suffers from significant uncertainties. Recalibrated values are given in Table 3 together with other reported fluxes and VLA archival data. Data taken between May 1994 and January 1995 all show similar flux levels. Observations by Kurtz in 1989 and by Walsh in 1994 both show smaller fluxes by about a factor of three to four. The flux

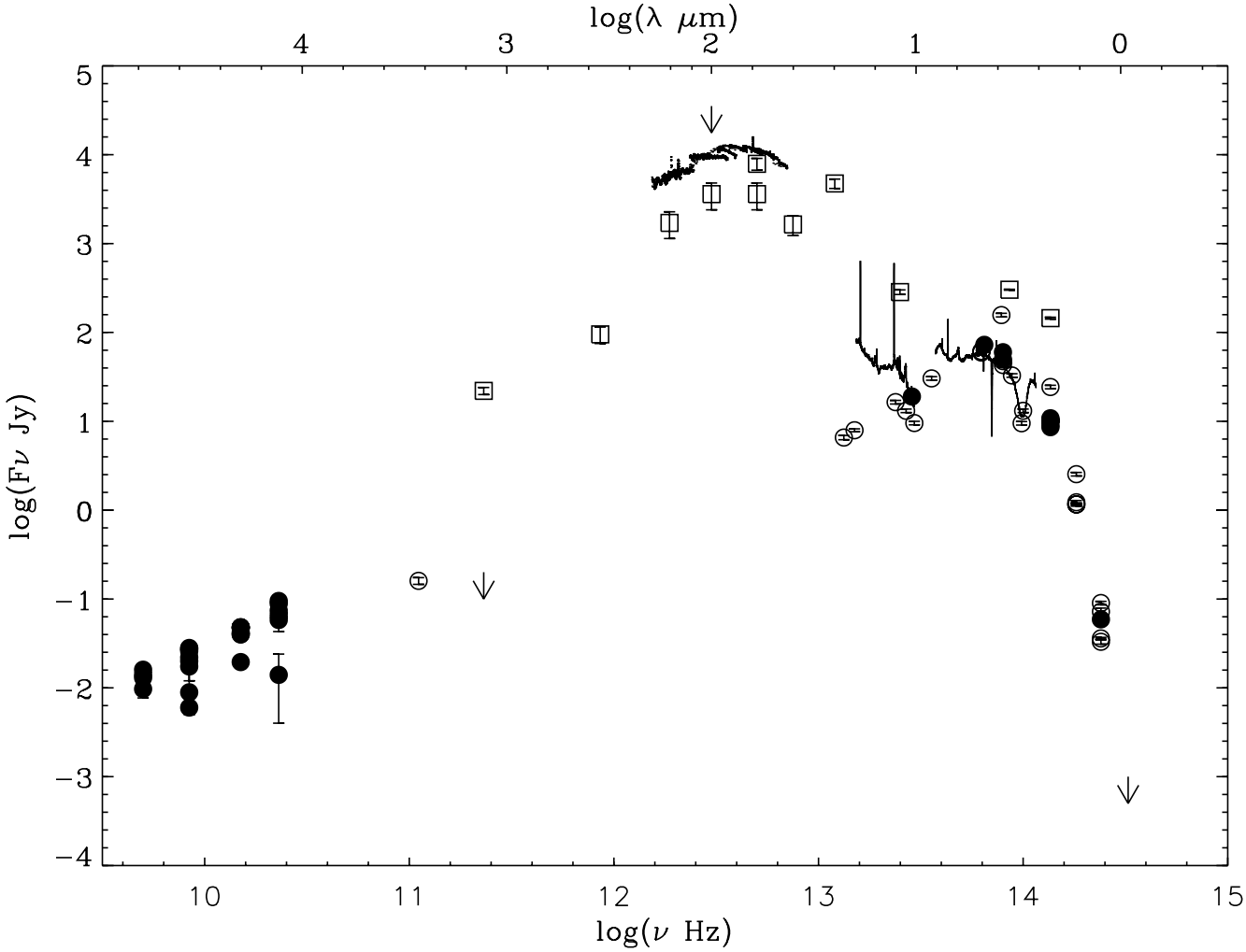

Fig. 4. The spectral energy distribution of IRS2, compiled from published photometric data and ISO SWS/LWS spectra. Details concerning these data are given in Tables 2–4. The high resolution ISO spectra (shown as continuous lines) are obtained in AOT6 mode. Open squares denote measurements made with apertures larger than 40″; open circles indicate aperture sizes of 5–20″; closed circles represent beam sizes less than 5″. Most often, the error bars on the data are smaller than the symbol size. The subdivision in aperture size clearly shows that the emission bump peaking at about 100 μm is not due to the nearby circumstellar medium of IRS2, i.e. it is not associated with the system itself but must come from warm material in the vicinity of the star.

differences cannot be attributed to differences in beam size. Radio variability and spectral index is discussed in Sect 4.1.

We conclude that the bulk of the mid- and far-infrared emission observed in large apertures and peaking at ~100 μm is *not* associated with the nearby circumstellar medium of IRS2, but arises from a more diffuse source. Therefore, one cannot use the IRAS color-color criteria for UCHII regions (Wood & Churchwell 1989) to conclude that IRS2 is a massive star surrounded by a dust cocoon. This weakness of the infrared criterion for UCHII was already pointed out by Codella et al. (1994) and Ramesh & Sridharan (1997). Except for the shortest infrared wavelengths, only small aperture observations (≤20″) are relevant in probing the nature of IRS2 and its immediate circumstellar environment. Large aperture measurements will not be considered further in this paper.

3.2. Extinction

Estimates for the extinction towards IRS2 are very uncertain and range between A_V = 12 and 32 mag (Thompson et al. 1981; Grasdalen 1974). The identification of IRS2b as the ionizing source of the Flame Nebula, 5″ away from IRS2 (Bik et al. 2003), allows for the first time an independent determination of the interstellar extinction caused by the elongated structure obscuring the center of NGC 2024. Applying the synthetic extinction law of Cardelli et al. (1989), Bik et al. (2003) find an A_V of 24 ± 0.5 mag towards IRS2b, taking R_V = 5.5. Note that the value of R_V is relevant for the absolute value of the extinction, but has only a weak effect on the slope of the near-infrared spectrum. IRS2 and IRS2b are most likely located in the H II region behind the cold obscuring dust bar and in front of a warm molecular cloud (Barnes et al. 1989). The 2.08−2.18 μm

spectrum of IRS2b does not show any evidence of circumstellar extinction (Bik et al. 2003), implying that the obscuration is dominated by the cold foreground molecular cloud.

To compare the interstellar extinction towards IRS2 and IRS2b, we have inspected the strength of the 3.0 μm water ice absorption seen towards both sources. Whittet et al. (1988) and Teixeira & Emerson (1999) present evidence for a linear relation between the optical depth in the ice band and the visual extinction. The parameters of this relation is expected to depend on the physical and chemical properties of the intervening medium, and thus may vary from cloud to cloud. The main uncertainty in the extinction determination is the uncertainty in the continuum flux level near the ice feature. The top panel of Fig. 5 shows normalized L-band spectra of both IRS2 and IRS2b. The spectrum of IRS2 stops at 3.5 μm due to saturation effects; that of IRS2b extends out to 4.0 μm. IRS2 has been observed by ISO/SWS. This allows a reliable determination of the continuum in our L-band spectrum, as the ISO spectrum covers a much broader wavelength interval. The normalization of the spectrum of IRS2b is problematic. First, the spectrum starts at 2.9 μm, which is somewhat inside of the ice feature. Therefore, we cannot use the short wavelength side of the profile to define the continuum. Second, just outside of the feature at the long wavelength side the spectral slope shows a kink at about 3.5 μm. We consider the two limiting cases: IRS2b1, in which the continuum is based on a slope measurement in the 3.4 to 3.5 μm region, and IRS2b2, in which the continuum is derived from the 3.5 to 4.0 μm interval. The lower panel of Fig. 5 shows the ratio of the L-band spectra of IRS2 and IRS2b for these two cases.

For both normalizations the ice band absorption in IRS2 is found to be stronger than in IRS2b, showing that more interstellar ice is present in the line of sight towards IRS2. Using $A_V = 24$ mag for IRS2b, we arrive at a propotional A_V of 27 (using IRS2b1) to 41 mag (using IRS2b2) for IRS2. If we require an intrinsic spectral index of two, the upper limit can be adjusted down to $A_V = 36.5$ mag (for $R_V = 5.5$). We conclude that the visual extinction towards IRS2 is between 27 and 36.5 mag.

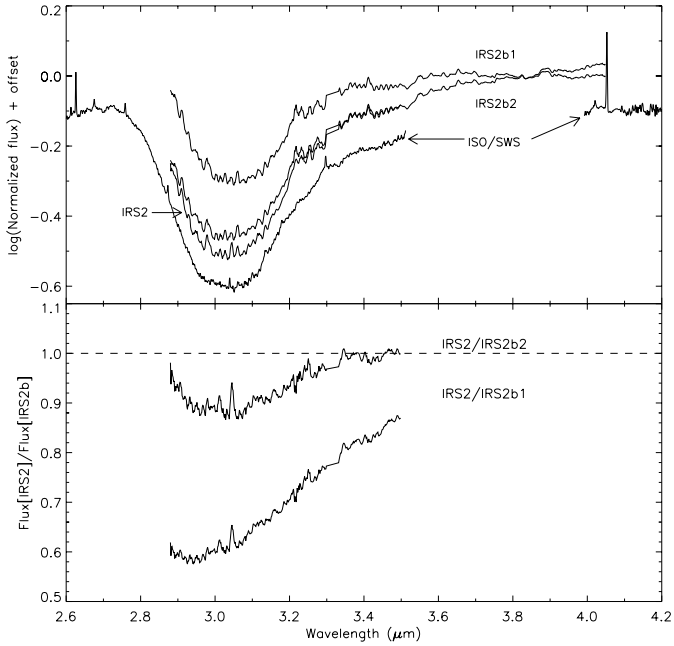

Fig. 5. The upper panel shows the 3.0 μm ice band in the normalized L-band spectra of IRS2b and IRS2, as well as the normalized ISO/SWS spectrum of IRS2 (shifted by −0.1). IRS2b is normalized using the slope of the 3.4 to 3.5 μm region (denoted IRS2b1) and of the 3.5 to 4.0 μm region (IRS2b2). The lower panel shows the ratio of the ice feature in IRS2 and in IRS2b, indicating that the extinction towards IRS2 is higher.

4. Diagnostic tools

We discuss a number of independent diagnostic methods that may help to constrain the geometry of the circumstellar material around IRS2. First, we use the radio slope to determine the gradient in the radial density structure. We compare this slope with values typical for spherical outflows and disks. Second, we apply a technique developed by Lenorzer et al. (2002a) in which the flux ratio of lines in the L'-band are used to determine whether the material is distributed in a spherically symmetric or disk-like structure. Third, we briefly summarize the important observational and modeling findings made on CO band-head emission about IRS2.

4.1. Radio slope

The radio observations are listed in Table 3 (in appendix) and plotted in Figs. 6 and 7. Discarding the problematic points taken in 1981−83 (Snell & Bally 1986) and 1989 (Gaume et al. 1992) (see Sect. 3), flux variations of up to about a factor of three are observed on timescales of years, and variations of roughly a factor of two on timescales of months. Data prior to 1994 indicate relatively low flux densities, whereas the 1994−1995 dataset suggests a significant brightening of the source, followed by a possible relaxation in 2002. The nature of this variability is not understood, however it may suggest some sort of flaring event. The spectral indices $\alpha \equiv \partial \log \mathcal{F}_\nu / \partial \log \nu$ derived from simultaneous measurements suffer from large uncertainties, but do not show a trend in time, nor do they depend on frequency base. Simultaneous observations yield spectral indices ranging from 0.75 to 1.33, with a weighted average of $\alpha = 1.25 \pm 0.06$.

The radio spectral index can be used as a diagnostic of the density structure in a circumstellar medium. For a spherical, isothermal stellar wind that has reached its terminal velocity it can be shown (Wright & Barlow 1975; Panagia & Felli 1975; Olnon 1975) that $\alpha = 2/3$, neglecting a very modest dependence of the Gaunt III factor on frequency. The observed slopes are somewhat steeper, suggesting either that the ionized region is sharply bounded (Simon et al. 1983), or that the radial density distribution $\rho(r) \propto r^{-m}$ has a gradient steeper than that for a constant velocity wind, $m = 2$. For the wind model described in Sect. 5 with $m = 2$, two free parameters essentially determine the radio spectrum: the electron density at the stellar surface and the recombining radius. Recent observations by

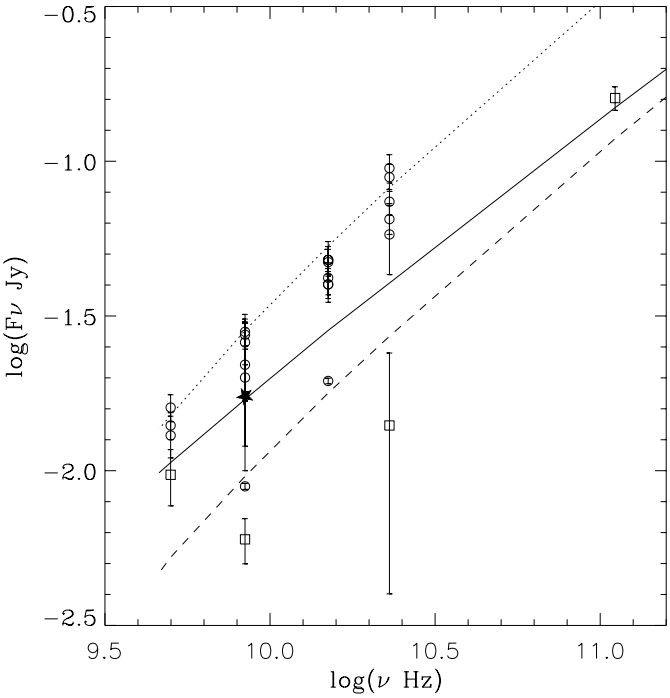

Fig. 6. Radio observations of IRS2. Multi-frequency observations at a single epoch are denoted by open circles. Squares represent non simultaneous data. Recent observations by Rodríguez (priv. comm.) resolving the radio source are denoted by a filled star. Assuming a spherical wind, these data are fitted by $n_0 = 10^{11}$ cm^{-3} and $R_{\rm out} = 145$ AU. Data point obtained at other epochs yield roughly similar parameters: 1989 observations by Kurtz et al. (1994) imply the same n_0 and $R_{\rm out} = 25$ AU (dashed line); (1994) and (1995) data require $n_0 = 2.5 \times 10^{11}$ cm^{-3} and recombination at 42 AU (dotted line).

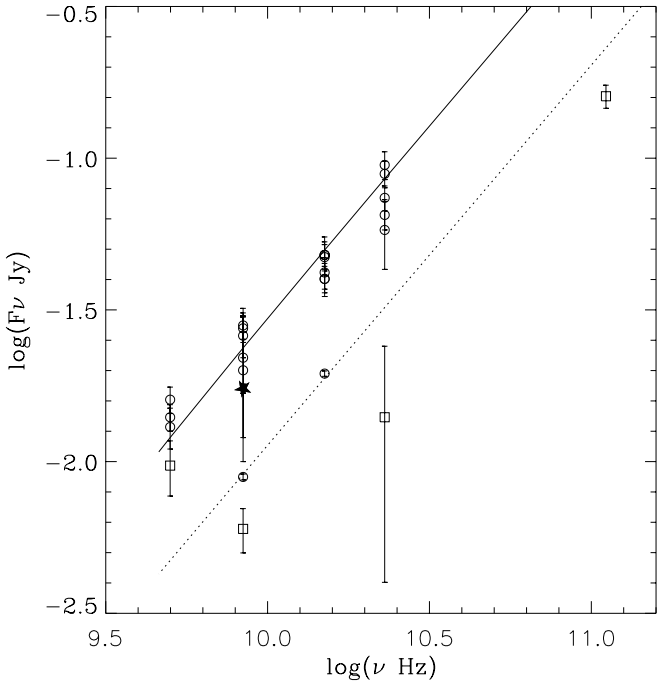

Fig. 7. Same data as in Fig. 6. Here the overplotted models are for disks. We fit the radio observations of IRS2 with a disk model. Both models are for a slope of $m = 3.17$ in the radial density distribution. The solid (dashed) line assumes an electron density at the stellar surface of 6.7 (1.8) $\times 10^{16}$ cm^{-3} and an outer radius of 77 (39) AU, respectively, to prevent a turn-down of the radio spectrum.

Rodríguez (priv. comm.) have resolved the radio source, its diameter is 0.8″ at 3.6 cm, corresponding to a radius of 145 AU. This outer radius and the flux measured by Rodríguez require an electron density of $n_0 = 10^{11}$ cm^{-3} (solid line in Fig. 6). Data obtained at different epochs are matched by roughly similar combinations of outer radius and n_0 (see also Fig. 6).

In the more general case that a spherically symmetric density distribution is given by a power-law, the spectral index is given by $\alpha(m) = (4m - 6)/(2m - 1)$ where again the Gaunt III dependence on frequency is neglected. To match the observations one finds $m = 3.17$ for $\alpha = 1.25$. The $\alpha(m)$ relation also holds when the gas is in a disk with a constant opening angle, if the density still has a symmetric radial dependence. Disk models applied to different epochs are presented in Fig. 7 for an opening angle of 5 degrees. The free parameters of these models are (again) the electron density at the stellar surface and the disk radius. The electron density required to match the flux density is high (between 1.8 and 6.7×10^{16} cm^{-3} at the stellar surface). Waters et al. (1991) observed six classical Be-stars at millimeter wavelengths and found their spectral indices to be in the range $0.94 \leq \alpha \leq 1.45$. These values are comparable to the ones for IRS2. However, typical densities for these "classical disks" are several orders of magnitude lower than what is required for IRS2.

The present data do not allow us to conclude whether the observed radio variability is due to changes in the ionization and/or density structure. In Sect. 5 we will use the overall SED to further constrain the circumstellar environment.

4.2. Infrared hydrogen recombination lines

Lenorzer et al. (2002a) recently developed a tool to investigate the geometry of the circumstellar material around hot stars. A diagram using hydrogen lines from different series, all observable in the L'-band, allows one to separate sources in which the circumstellar material is distributed roughly spherically (e.g. LBV stars) from sources in which it is more disk-like (e.g. Be stars). The diagram (Fig. 8) is based on 21 spectra obtained by ISO/SWS (Lenorzer et al. 2002b). It shows that both line flux ratios Hu(14-6)/Pfγ and Hu(14-6)/Brα increase from LBV to B[e] to Be stars. This trend can be understood in terms of the span in absorption coefficients of these lines. In an optically thin medium one expects the flux ratios to follow Menzel Case B recombination theory. At the other extreme, in an optically thick medium, the ratios become independent of the absorption coefficient as the flux in any line is determined by the size of the emitting surface. Some limitations of this diagnostic tool are to be expected, as the correlation between geometry and optical depth is established from objects for which the geometry of the circumstellar material is reasonably

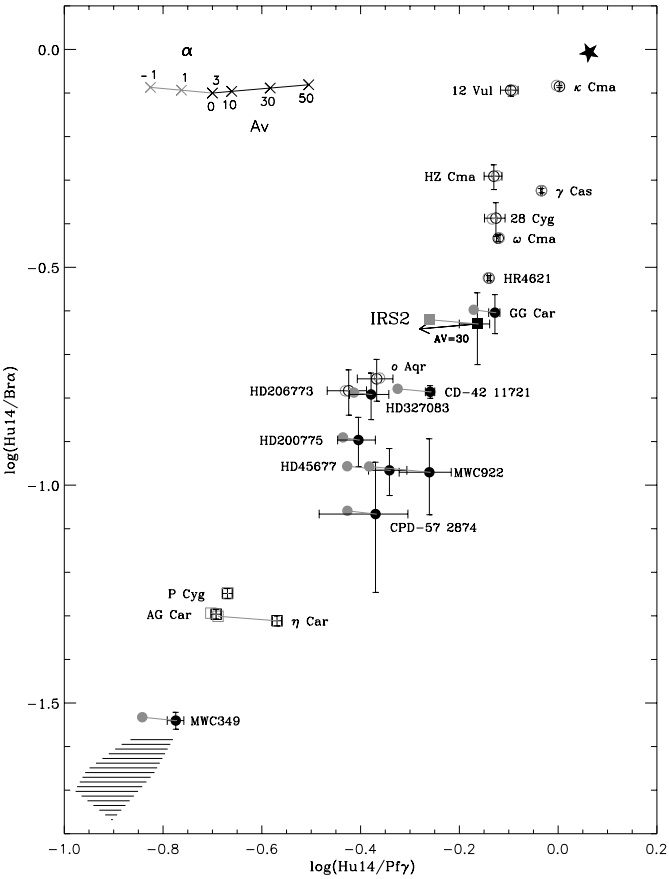

Fig. 8. Hu(14-6)/Brα versus Hu(14-6)/Pfγ for hot stars observed with ISO (Lenorzer et al. 2002b). The different classes of objects, LBVs (squares), B[e] stars (filled circles) and Be stars (open circles) are well separated. IRS2 is denoted by a filled square. The filled asterisk indicates the position of optically thick black-body emission; the striped region shows the range for Menzel case B recombination, including collisional de-excitation, for temperatures higher than 10^4 K. Line flux ratios are plotted in black; *EW* ratios in grey.

simple. Deriving the geometry of objects that might have multi-components and vary on short timescales is not trivial and requires additional diagnostics, e.g. the modeling of the line profiles.

To investigate the effect of extinction the diagram includes the line flux and *EW* ratios. The *EW* diagram is calibrated on the line flux diagram such that P Cygni, which has negligible extinction, is at the same location in both diagrams. Figure 8 shows that IRS2 falls in the upper right part of the diagram, close to the B[e] star GG Car. This position indicates that its lines are predominantly formed in optically thick gas. This situation likely arises in a disk-like geometry. The position of the line flux ratio of IRS2 corrected for an A_V of 30 mag (Sect. 3.2) is also indicated in the figure. There is a close agreement between the de-reddened line flux ratio and the *EW* ratio of IRS2. The large shift observed for B[e] stars is not predominantly caused by extinction (all plotted sources have very moderate A_V), but by a rising dust continuum reducing their spectral indices. We conclude that the continuum of IRS2 is not affected by a dust continuum strongly rising between 3.74 and 4.05 μm.

To further constrain the geometry of the circumstellar material, we investigate the line widths. The Humphreys lines as well as the Pfγ line have *FWHM*s of about 400 km s^{-1}; the *S/N* of the L'-band spectrum is too low to derive any trend in the widths of these lines. The Brackett lines are narrower with *FWHM*s of about 200 km s^{-1} (Sect. 2.2), suggesting a different line forming region for intrinsically stronger lines.

The ratio of the *FWHM*s of Pfγ and Brα is about 2.0. For typical Be stars like γ Cas, HR4621, κ Cma or in the B[e] star GG Car, close to the position of IRS2 in the diagram, this ratio lies between 1.1 and 1.3, whereas it is less than 1.0 for wind sources like P Cyg. The fact that the Brackett lines are much narrower than the other hydrogen lines suggests that they have a significant contribution from low density gas close enough to the star to be observed in our narrow-slit spectrum. The *FWHM* of this optically thin component can be estimated from the high-resolution spectrum of the Brγ line as $\leq$130 km s^{-1}. The infrared recombination lines observed in IRS2 are mainly produced in a high velocity (400 km s^{-1}) optically thick medium, with a small contribution from a lower velocity ($\leq$130 km s^{-1}) optically thin medium. The high velocity contribution in itself would give IRS2 a position in Fig. 8 that is closer to the Be stars.

4.3. CO band-heads

CO band-head emission at 2.3 μm was first detected in NGC 2024/IRS2 by Geballe et al. (1987). Its presence attests of the existence of high-density and warm molecular gas. CO is largely dissociated at $T \gtrsim 5000$ K, while for $T \lesssim 2000$ K the upper vibrational levels will not be excited frequently by collisions. In addition to the proper temperature range, a density of at least 10^{10} cm^{-3} is required to maintain the population of the excited vibrational levels, which radiatively decay rapidly via fundamental band transitions. The 2−0, 3−1, 4−2 and 5−3 band-heads were observed by Geballe et al. at a resolution of ~460 km s^{-1}, insufficient to resolve the individual CO lines. From the relative band-head intensities they estimated an excitation temperature of about 4000 K. From the intensity of the 2−0 band-head they found a minimum area of the CO line emitting region of 2.8×10^{24} cm^2, assuming that the lines close to the band-heads are optically thick.

Chandler et al. (1993, 1993) observed the 2−0 band-head at high spectral resolution and proposed two models to explain the observations: an accretion disk and a neutral wind. The accretion disk model requires an extinction in the *K*-band of about 4.4 mag, corresponding to $A_V \sim 33.0$ mag (for $R_V = 5.5$). The best fit values in the case of a disk are: an inclination angle of 33 degrees (i.e. rather face on), and $\dot{M}_{acc} = 5 \times 10^{-7}\ M_\odot$ yr^{-1}. Assuming a stellar mass of 15 $M_\odot$ the emission arises between 60 and 180 $R_\odot$ where Keplerian velocities are 130−220 km s^{-1}. The wind model requires a mass-loss rate of about $10^{-5}\ M_\odot$ yr^{-1} and maximum velocities of 100 to 500 km s^{-1}.

5. Discussion

In this section we discuss three simple configurations that may reproduce the observed SED and investigate their relevance based on the diagnostic tools presented in Sect 4. We evaluate the contribution of emission from an ionised wind and disk, as well as that of dust. We end the section with a discussion on the nature of IRS2.

For the emission from ionized gas we use a basic disk model, consisting of isothermal hydrogen in Local Thermodynamic Equilibrium (LTE) and consider bound-free and free-free emission. We assume the density distribution to be a power-law, i.e.

$$\rho(r) = \rho_0\,(r/r_0)^{-m} \qquad \text{or} \qquad n(r) = n_0\,(r/r_0)^{-m} \tag{1}$$

within the disk, where the density ρ and the electron density n have the value ρ_0 and n_0 at the stellar surface. The disk has a constant opening angle θ. The total bound-free and free-free optical depth for a beam passing the disk in the direction perpendicular to the mid-plane is given by

$$\tau_\nu^{\rm bf+ff}(T,r) = 2\,\kappa_\nu^{\rm bf+ff}(T)\int_0^{r\times\tan(\frac{\theta}{2})}\rho(r)^2\,{\rm d}z. \tag{2}$$

It follows that in the part of the spectrum produced by a partially optically thick medium, the spectral index is given by $\alpha = (4m-6)/(2m-1)$ (see Waters 1986).

We adopt an opening angle of $\theta = 5$ degrees, consistent with the small opening angles derived from spectropolarimetric observations of gaseous disks around classical Be stars (e.g. Putman et al. 1996). Note that this parameter influences the flux level similarly to ρ_0. The adopted gas temperature is 10 000 K. The free parameters of this model are then the density at the stellar surface ρ_0, the density gradient index m, and the outer radius of the disk $R_{\rm disk}$. The density parameter ρ_0 fixes the total flux while m determines the spectral index. The outer radius sets the wavelength at which the break occurs in the spectral index. The spherical wind model is very similar to the disk model, except for the difference in geometry, and the use of a fixed density gradient $m = 2$. We remark that for a dense disk the assumption of an isothermal medium is likely to break down, leading to lower temperatures in the midplane region as a result of self-shielding. This is not expected to change the predicted disk energy distribution significantly as this is set by emission from the disk surface layers, which can be illuminated directly and therefore have a high temperature. Finally, dust emission, which cannot arise in the ionized region, is modeled as black-body emission at temperature $T_{\rm d}$.

There is very little known about the stellar content of IRS2. From radio observations of the compact radio source associated with IRS2, Kurtz et al. (1994) derive an ionizing source corresponding to a B3 V star. K-band spectroscopy is consistent with an early B star. In the following, we assume the central object is a single early-B main-sequence star.

5.1. Model A: A gaseous disk

We first consider the case in which the entire spectral energy distribution is produced by one gaseous component (i.e., no dust). This model requires an interstellar extinction high enough to account for the sharp turn down observed at near-infrared wavelengths. This is achieved for $A_{\rm V} \geq 31.5$ mag. After dereddening, the best fit to all data points yields a spectral slope $\alpha = 1.09$, corresponding to a density gradient $m = 2.7$. The steep gradient favors a disk-like geometry. Matching the overall flux level requires an electron density $n_0 = 10^{15}$ cm^{-3}. The radio data do not show a break in the spectral index down to 6 cm, implying an outer radius of at least 100 AU. The best fit model is plotted in the top panel of Fig. 9. The model corresponds to a hydrogen disk mass of $M_{\rm disk} = 3.0 \times 10^{-6}\,M_\odot$ and a disk luminosity $\log(L_{\rm disk}/L_\odot) = 4.6$.

To investigate if such a very dense gaseous disk allows the excitation of CO band-heads, as is observed, we determine self-consistently the temperature throughout the disk using a technique developed by Millar & Marlborough (1998). This method adopts a Poeckert-Marlborough disk model assuming hydrostatic equilibrium. The continuity equation fixes the radial density gradient (see Marlborough 1969 and Poeckert & Marlborough 1978). The state of the gas is solved subject to statistical and radiative equilibrium. The final result is a set of self-consistent temperatures. For additional details of the temperature calculation we refer to Millar & Marlborough (1998, 1999a, 1999b) and Millar et al. (2000).

The adopted parameters are $n_0 = 3.33 \times 10^{14}$ cm^{-3} in the equatorial plane at the stellar surface and a scale height rising from 0.1 $R_\star$ at the stellar surface to 34.75 $R_\star$ at a radial distance of 100 $R_\star$. Note that this disk structure is somewhat different from that of our simple model, but close enough for the qualitative purposes. Figure 10 shows the temperature structure calculated for a central star having $T_{\rm eff} = 25\,000$ K, $R_\star = 10\,R_\odot$, and $\log g_\star = 3.67$ (representative of a B1 V star). The global-average kinetic temperature of the disk gas is 13 700 ± 4000 K. The temperature at the surface of the disk decreases from 15 000 K close to the star to 12 000 K over most of the surface. Mid-way between disk surface and equatorial plane the temperature rises above that of the surface. At radial distances beyond 15 $R_\star$ the temperature reaches approximately 17 000 K. In the equatorial plane however, the temperature drops drastically at around 10 $R_\star$ from 20 000 to 5000 K, decreasing outwards to 3000–4000 K. This is due to a large optical depth for photo-ionizing stellar radiation. Note that our detailed temperature computation assumes a pure hydrogen disk. Additional and more efficient cooling from metals and molecules at these temperatures would likely result in even lower temperatures. It is therefore plausible that the observed CO band-heads, representative of a 4000 K medium, originate from inside a *dense* gaseous disk. The observed CO emission does not necessarily require the molecules to be shielded by a dusty medium. The position of IRS2 in the line-flux ratio diagram (see Fig. 8) can be explained qualitatively with a massive Be-like disk, the shape of the lines, however, require a more complex geometry.

Model A is fairly compatible with the diagnostic tools discussed in Sect. 4, namely the observed radio slope, the infrared hydrogen recombination lines and CO band-heads, as well as with the extinction determination. The main shortcoming of this model is that it overestimates the observed mid-infrared

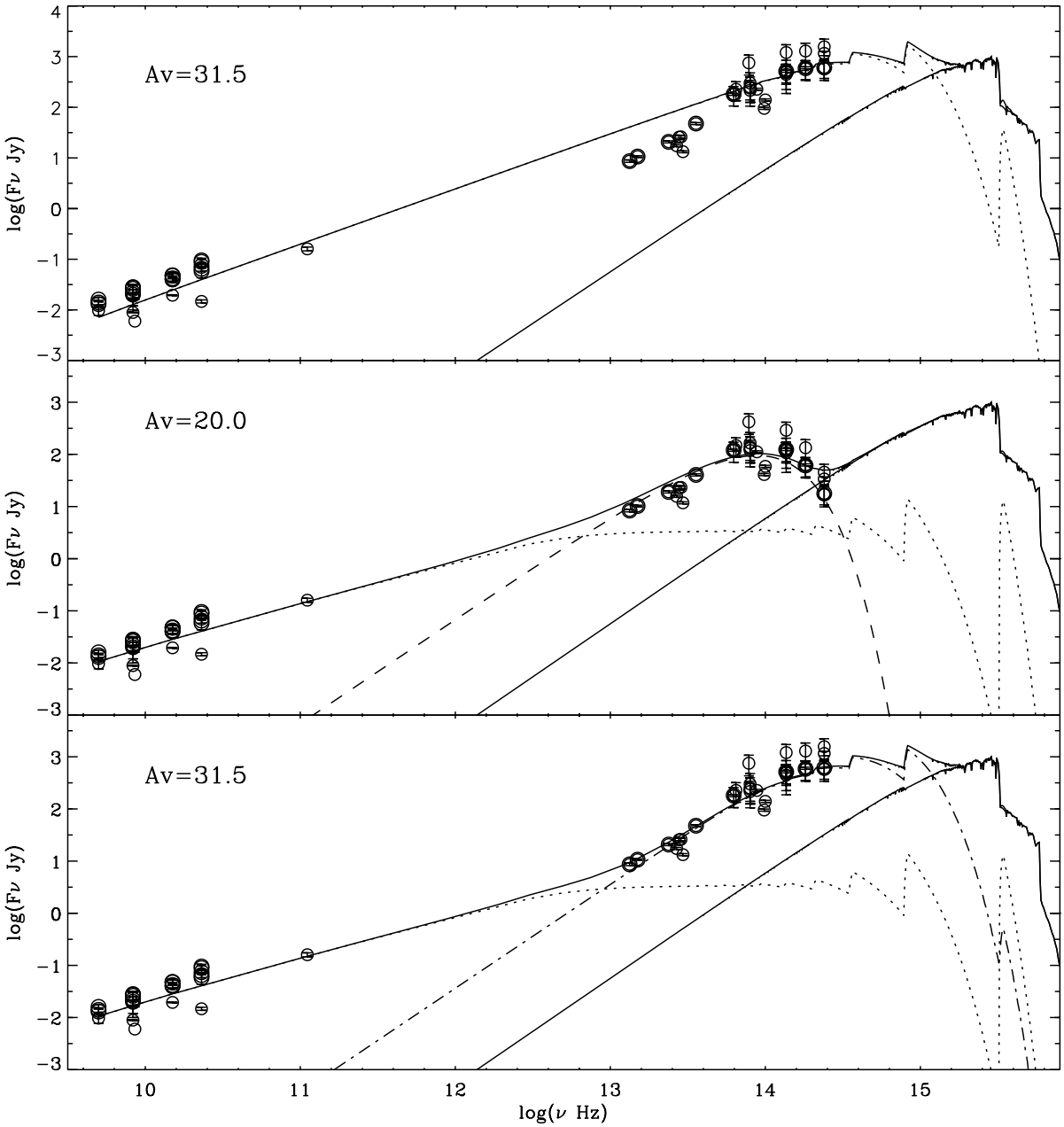

Fig. 9. Three models describing the circumstellar medium of IRS2. The central star is represented by a Kurucz model of $T_{\rm eff}$ = 33 000 K and $\log(L/L_\odot)$ = 4.87 (solid line). The observations are denoted by circles Note that the observations are de-reddened using a lower extinction in the middle panel ($A_{\rm V}$ = 20 instead of 31.5 mag). From top to bottom: Model A: the dotted line is the disk model and the thick solid line is the sum of the stellar and disk contributions; Model B: the dotted line is the wind model, the dashed line is the dust model and the thick solid line is the sum of the stellar, dust and wind contributions; Model C: the dotted line is the wind model, the dashed line is the disk model and the thick solid line is the sum of the stellar, disk and wind contributions.

flux in the 8−20 micron range. Also, the disk luminosity is a sizeable fraction of the luminosity of a main sequence star (about 50%). For an active disk, i.e. a disk that has an extra source of heating, (e.g. from accretion) this fraction would decrease. To get a rough idea, for a star of 15 $M_\odot$ and an accretion radius of 10 $R_\odot$, the disk luminosity corresponds to an Eddington accretion rate of the order of 10^{-3} $M_\odot$ yr^{-1}. Such accretion rates may perhaps occur in hot molecular cores, but seem unrealistically high for IRS2.

5.2. Model B: A stellar wind and optically thin dust

In the model discussed above, we assumed that one component is responsible for the entire SED. As can be seen from Fig. 9, Model A overestimates the mid-infrared flux. This wavelength range is also observed to have a spectral index of about 2, different from the radio range. In Model B we ascribe much of the infrared continuum emission to a different origin than the radio emission, i.e. we assume the radio flux to originate in a

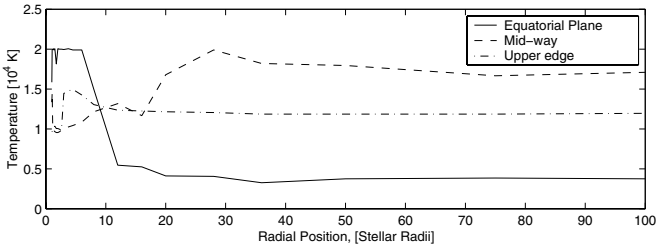

Fig. 10. The temperature structure for a Poeckert-Marlborough disk with $n_0 = 3.33 \times 10^{14}$ cm^{-3} in the equatorial plane at the stellar surface. Temperature profiles for three different heights above the equatorial plane are given. This calculation shows that CO band-head emission may arise in a dense gaseous disk.

dense ionization bounded wind, while a dust shell gives rise to the near- and mid-infrared flux.

In the middle panel of Fig. 9, we show a wind model with an electron density at the stellar surface of $n_0 = 10^{11}$ cm^{-3} and outer radius of 145 AU by a dotted line (cf. Sect. 4.1). The mass of hydrogen contained in this wind is $M_{\rm wind} = 7.6 \times 10^{-7}\ M_\odot$ yielding a mass-loss rate of about $\dot{M} = 1.1 \times 10^{-6}\ M_\odot$ yr^{-1} (adopting a terminal wind velocity of 1000 km s^{-1}). This mass-loss rate is about four times larger than predictions for early-B main-sequence stars by Vink et al. (2001). Assuming Baker & Menzel (1938) Case B, we find that the above wind density structure and outer (recombination) radius are appropriate for a B1 V star adopting ionizing fluxes by Panagia (1973).

We model the near-infrared part of the SED by a simple black-body. Strictly speaking, this is only allowed if the dusty medium is optically thick. However, for dust temperatures near 1500 K (which are required; see below) dust extinction will be dominated by species that have a rather grey extinction behaviour at near-infrared wavelengths, such as carbon grains. In that case, the assumption of black-body emission also holds for an optically thin, isothermal dusty medium. The monotonic slope of the SED in the 5−20 μm region is quite insensitive to extinction and shows that if dust is to contribute, it must have a temperature higher than 1000 K. The highest dust evaporation temperatures are around 1500 K and result in a peak flux density at 3.4 μm. To have the flux peak at this wavelength requires an $A_{\rm V}$ of 20 mag; cooler dust requires less extinction. This extinction is less than the derived minimum extinction towards IRS2 of 27 mag. Any contribution to the extinction by circumstellar dust only aggravates the problem. To minimize the extinction problem we model the dust emission using a blackbody of 1500 K (see dashed line in middle panel of Fig. 9). The properties of the central star require this dust to be at about 240 stellar radii. The observed flux density at near-infrared wavelengths then implies that this dust is optically thin. The single temperature blackbody is slightly broader than the observed emission, a problem that cannot be solved using a temperature distribution to represent the dust as that would only broaden the emission further. A higher extinction (than $A_{\rm V} = 20$ mag) allows a broader intrinsic near- and mid-IR flux distribution. However, it would simultaneously shift the peak emission towards shorter wavelengths. This would require dust at temperatures in excess of 1500 K, which is not physical.

The near-infrared hydrogen recombination lines could, in principle, originate in a recombining wind with parameters similar to those derived above and an $A_{\rm V}$ of 20 mag (Maihara et al. 1990). The main problem of model B is that it is incompatible with the minimum extinction of 27 mag towards IRS2. For this reason the optically thin hot dust model proposed by Jiang et al. (1984) cannot be supported.

5.3. Model C: A wind plus a gaseous disk

Finally, we consider a model in which the radio emission originates in a recombining wind, and the infrared component in a gaseous disk. The wind component has the same characteristics as in Model B. Matching the mid-infrared part of the SED with a gaseous disk requires an extinction of 31.5 mag, similar to Model A. The mid-infrared spectral index is close to $\alpha = 2$, i.e. to the value expected for an optically thick isothermal medium The dereddened mid-IR observations can be fitted by a black-body of at least 5000 K, the flux level constraining the size (i.e. surface area) of this component. If the temperature is higher, the same extinction allows the near-infrared part of the SED to be partially optically thin.

Lacking a constraint on the density gradient, we use $m = 2.0$. We retain the disk geometry assuming an opening angle of 5 degrees and a temperature of 10 000 K. We obtain $n_0 = 1.8 \times 10^{14}$ cm^{-3} and an outer radius of $R_{\rm disk} = 140.0\ R_\odot$. This component is plotted in the bottom panel of Fig. 9 with a dashed line. It corresponds to $M_{\rm disk} = 2.5 \times 10^{-7}\ M_\odot$ and a $\log(L_{\rm disk}/L_\odot) = 4.5$.

The infrared recombination lines are easily explained by this model. The broad optically thick portions of the lines would originate in the disk and the optically thin contributions would be produced in the outer wind. The CO band-heads likely originate from the equatorial plane and outer part of the disk, as the high densities and low temperatures (due to the shielding) can provide the required physical conditions for the existence of CO and for excitation of the band-heads (see Sect. 5.1). This location is also in agreement with results of CO band-head modeling by Chandler et al. (1993) (see Sect. 4).

In conclusion, model C fulfills all the observational diagnostics and fits the observations best. Similarly to model A, model C implies a disk luminosity that is comparable to the stellar luminosity of a B0 V star for which $\log(L_{\rm disk}/L_\odot) = 4.86$ (Smith et al. 2002). In principle this is possible, though it implies that the total opening angle of the disk should be ~45 degrees. If we have underestimated the stellar luminosity then the disk could have a smaller opening angle. Alternatively, the disk could have an intrinsic energy source, e.g. as a result of accretion (cf. Sect. 5.1) providing (part of) the disk luminosity.

5.4. The nature of NGC 2024 IRS2

The location of IRS2 in the star-forming complex Orion B suggests it is a young object, perhaps even in a pre-main sequence stage of evolution. Objects similar to the

Becklin-Neugebauer (BN) object in Orion, which reside in cores of molecular clouds, have been proposed to represent deeply embedded massive YSOs. Therefore, we compare the properties of IRS2 with those of BN-like objects (see Henning & Gürtler 1986 for a review).

Both IRS2 and the BN-like objects are very compact sources in the near- and mid-IR as well as in the radio, with sizes of about 10 to 100 AU. For an A_V of 31.5 mag and the adopted distance of 363 pc, we find a minimum luminosity for IRS2 of 10^4 $L_\odot$, corresponding to a B0.5 V star. This is in reasonable agreement with that of the BN-like objects, which have integrated luminosities in the range of $\sim 10^3$ to 10^4 $L_\odot$. The near-IR hydrogen recombination lines in BN-like objects, like in IRS2, have extended wings (with *FWHM* of several hundreds of kilometers or more) and have flux ratios which are not consistent with Case B recombination. Also, both the BN-like objects and IRS2 show CO band-heads, implying dense and warm neutral gas. However, the BN-like objects show evidence for an optically thick dust cocoon as well as for a cold molecular surrounding. Both are absent in IRS2. Perhaps IRS2 is in a similar evolutionary stage as the BN-like objects, but somehow has its circumstellar cloud disrupted by another more evolved source (such as IRS2b). More likely, the star is more evolved. This would be supported by the apparent absence of dust in the system. If the disk in IRS2 would represent a remnant of the stellar formation process, one would expect dust to be present as it is a constituent of the molecular cloud material that is accreted.

6. Conclusion

We have investigated the near-infrared and radio source NGC 2024 IRS2/G206.543–16.347 focusing on K-, L' and L-band spectroscopy and on a reconstruction of the spectral energy distribution from near-IR to the radio wavelengths. The primary goal was to obtain better insight into the nature of the central star and its circumstellar medium. Simple models were used to test a number of diagnostics, notably the slope and flux level at radio wavelengths, the flux ratios of near-IR hydrogen lines, and the CO band-head emission.

Previously, IRS2 has been associated with the IRAS source 05393–0156, and, on the basis of this was found to satisfy the color-color criteria for UCHII regions. We show from beam-size arguments that the large infrared flux peaking around 100 μmdoes not originate from a dusty cocoon confining the ionized gas around IRS2, but rather from a background. This is consistent with the offset of 72.8 between IRS2 and the IRAS source 05393–0156. Therefore, IRS2 may not be interpreted as a "cocoon" star, i.e. as the object usually depicted as an UCHII region.

To gain a better understanding of the nature of the circumstellar medium we compared our observations with a number of relatively simple models: a dense gaseous disk; a stellar wind plus a dust shell; and a stellar wind plus a gaseous disk. The last model fits the observational constraints best. New spectra and the models allow one to draw a number of conclusions concerning the properties of the central star and of the ambient medium of IRS2. These conclusions are:

1. Both the radio flux and the 2.08−2.18 μm spectrum are consistent with an early-B spectral type for the central star.
2. Based on a comparative study of the ice-band optical depth in IRS2 and in IRS2b the visual extinction towards IRS2 is constrained to be between 27 and 36.5 mag, with a preference for an A_V of 31.5 mag based on the shape of the SED.
3. The presence of dust cannot be completely excluded, although emission from dust cannot be the dominant source of radiation in the infrared. A Significant amount of dust can only be present in the equatorial plane of an optically thick gaseous disk, where it would be unable to contribute much to the infrared spectrum.
4. The infrared recombination lines observed in IRS2 originate for the most part in a high velocity (400 km s^{-1}) optically thick medium, likely distributed in a disk, and to some extent in a lower velocity ($\leq$130 km s^{-1}) optically thin medium.
5. Mg II and possibly Fe II lines are observed, implying the presence of a dense and warm medium with velocities of about (400 km s^{-1}), similar to the hydrogen lines.
6. The CO band-head emission originates in a high density region, where the temperature must drop to about 4000 K and where velocities are about 200 km s^{-1}. For such relatively low temperatures to arise close to the star requires shielding. We have shown that this shielding may be provided by high density gas located within some ten stellar radii from the star.
7. The radio data are best described by a stellar wind model with a mass-loss rate of 1.1×10^{-6} $M_\odot$ yr^{-1} recombining at 145 AU. The radio emission is variable on short timescales (months), its spectral index might also vary. These variations may be explained by changes in the ionization and/or density structure; however, non-thermal radiation cannot be excluded.
8. The origin of the infrared SED is best described by a high density disk-like gaseous medium that is optically thick in the mid-infrared and extends to about 15 $R_\star$.
9. The luminosity emitted by the circumstellar material is comparable to the total luminosity of an early-B main-sequence star. It is possible that either the star has a higher luminosity, which would be consistent with the high mass-loss rate derived from radio observations, or part of the luminosity is supplied by the disk e.g. through accretion.

Acknowledgements. We would like to thank the Observatory Staff of UKIRT and of the VLT. We are grateful to L. Decin for her help in the data reduction, to S. Hony and C. Neiner for useful and repeated discussions. M. Marlborough and A. Sigut are acknowledged for their help with the temperature model. We thank R. Gaume for his willingness to share the archival VLA data. UKIRT is operated by the Joint Astronomy Centre on behalf of the UK Particle Physics and Astronomy Research Council. TRG's research is supported by the Gemini Observatory, which is operated by the Association of Universities for Research in Astronomy on behalf of the international Gemini partnership of Argentina, Australia, Brazil, Canada, Chile, the United Kingdom, and the United States of America.

7. Appendix

Table 2. Small aperture data used to construct the spectral energy distribution: we list the observing date, frequency, wavelength, beam size, magnitude, flux, observational technique when not photometric, and reference.

Date	ν	λ	Beam	Magnitude	Flux	Tech	Ref.
	10^{12} Hz	(μm)	($''$)		(Jy)		
1976–77	326	0.92		≥16.5	≤0.001	(a)	F79
1974	240	1.25	≤12	10.80 ± 0.10	0.072 ± 0.007		G74
1982	240	1.25	10	11.64 ± 0.05	0.033 ± 0.002		B89
1986	240	1.25	15	11.57 ± 0.02	0.036 ± 0.001		C86
1991	240	1.25	15	10.56 ± 0.05	0.090 ± 0.004		N94
1999	240	1.25	0.7 × 0.7	11.02 ± 0.15	0.059 ± 0.008	(b)	B03
1974	182	1.65	≤12	7.32 ± 0.05	1.226 ± 0.056		G74
1982	182	1.65	10	7.38 ± 0.05	1.160 ± 0.053		B89
1986	182	1.65	15	7.38 ± 0.02	1.160 ± 0.021		C86
1991	182	1.65	15	6.53 ± 0.05	2.538 ± 0.117		N94
1974	136	2.20	≤12	4.54 ± 0.05	10.423 ± 0.480		G74
1982	136	2.20	10	4.59 ± 0.05	9.954 ± 0.459		B89
1986	136	2.20	15	4.57 ± 0.02	10.139 ± 0.187		C86
1991	136	2.20	15	3.62 ± 0.05	24.322 ± 1.120		N94
1993	136	2.20	3.1 × 3.1	4.7 ± 0.2	8.995 ± 1.666		N94
1994	136	2.20	3.1 × 3.1	4.5 ± 0.2	10.814 ± 2.003		N94
1999	136	2.20	0.7 × 0.7	4.75 ± 0.1	8.590 ± 0.792	(b)	B03
1997	86–115	2.6–3.5	14 × 20		25–35	(c)	ISO
1974	100	3.00	≤12	3.76 ± 0.05	13.115 ± 0.604		G74
1974	98.3	3.05	≤12	4.08 ± 0.05	9.506 ± 0.438		G74
1974	88.2	3.40	≤12	2.54 ± 0.05	32.779 ± 1.510		G74
1982	79.7	3.76	10	2.06 ± 0.05	42.973 ± 1.980		B89
1986	79.7	3.76	15	1.95 ± 0.04	47.554 ± 1.752		C86
1993	79.7	3.76	3.1 × 3.1	1.7 ± 0.2	59.867 ± 11.090		N94
1994	79.7	3.76	3.1 × 3.1	1.9 ± 0.2	49.796 ± 9.225		N94
1991	78.3	3.83	15	0.62 ± 0.05	156.809 ± 7.224		N94
1997	37.5–74.9	4.0–8.0	14 × 20		40–70	(c)	ISO
1982	64.6	4.64	0.27 × 5	1.09 ± 0.03	72.489 ± 2.003	(d)	J84
1986	62.5	4.80	15	1.20 ± 0.04	61.609 ± 2.270		C86
1974	62.5	4.80	≤12	1.24 ± 0.05	59.380 ± 2.736		G74
1974	35.7	8.40	≤12	0.80 ± 0.05	30.367 ± 1.399		G74
1974	29.4	10.2	≤12	1.62 ± 0.05	9.552 ± 0.440		G74
1997	25.0–29.4	10.2–12.0	14 × 20		15–35	(c)	ISO
1998	28.6	10.5	1.5		19.000 ± 1.000		W01
1974	26.8	11.2	≤12	1.06 ± 0.05	13.119 ± 0.604		G74
1997	15.4–25.0	12–19.5	14 × 27		35–80	(c)	ISO
1974	2.3.8	12.6	≤12	0.54 ± 0.05	16.416 ± 0.756		G74
1974	1.5.0	20.0	≤12	0.19 ± 0.04	7.925 ± 0.292		G74
1974	1.3.3	22.5	≤12	0.09 ± 0.06	6.562 ± 0.363		G74
1986	0.231	1300	11		≤0.2	(e)	M88
1994	0.111	2700	8.2 × 7.7		0.1600 ± 0.0140	(e)	W95

Tech: (a): photography; (b): narrow-band photometry; (c): spectroscopy; (d): speckle interferometry; (e): interferometry.

Ref: G74: Grasdalen (1974); J84: Jiang et al. (1984); C86: Chalabaev & Léna (1986); S86: Snell & Bally (1986); B89: Barnes et al. (1989); G92: Gaume et al. (1992); K94: Kurtz et al. (1994); N94: Nisini et al. (1994); W95: Wilson et al. (1995); W98: Walsh et al. (1998); W01: Walsh et al. (2001); B03: Bik et al. (2003); ISO: *Infrared Space Observatory*, obtained in AOT6 mode.

Table 3. Small aperture interferometric data used to construct the spectral energy distribution at centimeter wavelengths. The listed quantities are the same as in Table 2.

Date	ν GHz	λ (cm)	Beam (″)	Flux (mJy)	Ref
Aug. 1994	23	1.3	0.3	88.8 ± 8.9	VLA
Oct. 1994	23	1.3	0.9	74 ± 7	VLA
Jan. 1995	23	1.3	2.8	65 ± 7	VLA
Apr. 1995	23	1.3	2.8	58 ± 15	VLA
Aug. 1995	23	1.3	0.08	95 ± 10	VLA
Nov. 1989	23	1.3	2.4	14.7 ± 10.0	G92
Mar. 1989	15	2	0.5	19.5 ± 0.4	K94
May. 1994	15	2	0.4	40 ± 5	VLA
Aug. 1994	15	2	0.4	47.2 ± 4.7	VLA
Oct. 1994	15	2	1.2	48 ± 5	VLA
Jan. 1995	15	2	3.9	48 ± 7	VLA
Apr. 1995	15	2	3.9	42 ± 5	VLA
Aug. 1995	15	2	0.14	40 ± 4.0	VLA
Mar. 1989	8.4	3.6	0.5	8.9 ± 0.2	K94
1994	8.4	3.6	1.0	6.0 ± 1.0	W98
May. 1994	8.4	3.6	0.7	26 ± 4	VLA
Aug. 1994	8.4	3.6	0.7	27.5 ± 2.8	VLA
Oct. 1994	8.4	3.6	2.3	22 ± 10	VLA
Jan. 1995	8.4	3.6	8.4	20 ± 10	VLA
Aug. 1995	8.4	3.6	0.24	28.1 ± 2.8	VLA
Mar. 2002	8.4	3.6	0.24	17.4 ± 0.6	R02
Nov. 1983	5	6	2.6	9.7 ± 2	S86
May. 1994	5	6	1.2	13 ± 2	VLA
Aug. 1994	5	6	1.2	16 ± 1.6	VLA
Aug. 1995	5	6	0.4	14 ± 1.4	VLA

Ref: S86: Snell & Bally (1986); G92: Gaume et al. (1992); K94: Kurtz et al. (1994); R02: Rodríguez (priv. comm. 2002); W98: Walsh et al. (1998); VLA: *Very Large Array* Archival Data.

Table 4. Large aperture data used to construct the spectral energy distribution: we list the same quantities as in Tables 2 and 3.

Date	ν 10^{12} Hz	λ (μm)	Beam (″)	Flux (Jy)	Tech	Ref
1976–77	136	2.20	62	144.76 ± 3.55		F79
1976–77	85.7	3.50	62	302.3 ± 3.55		F79
1983	25.0	12	45 × 270	284.4 ± 17.0		IRAS
1983	12.0	25	45 × 276	4746 ± 570		IRAS
1997	10.3–10.5	28.6–29	20 × 27	325–360	(c)	ISO
1997	7.89–10.3	29–38	20 × 33	520–940	(c)	ISO
1981–83	7.50	40	49	1640 ± 410		T84
1997	1.52–6.97	43–197	84	5000–15000	(c)	ISO
1981–83	5.00	60	49	3600 ± 1200		T84
1983	5.00	60	90 × 282	7894 ± 1200		IRAS
1981–83	3.00	100	49	3600 ± 1200		T84
1983	3.00	100	180 × 300	≤35 330		IRAS
1981–83	1.87	160	49	1710 ± 570		T84
1985	0.857	350	90	95 ± 20		M88
1985	0.231	1300	90	22 ± 2		M88

(1) (c): spectroscopy
(2) T84: Thronson et al. (1984); F79: Frey et al. (1979); M88: Mezger et al. (1988); IRAS: *Infrared Astronomical Satellite*; ISO: *Infrared Space Observatory*.

References

Baker, J. G., & Menzel, D. H. 1938, ApJ, 88, 52
Barnes, P. J., Crutcher, R. M., Bieging, J. H., Storey, J. W. V., & Willner, S. P. 1989, ApJ, 342, 883
Bik, A., Lenorzer, A., Kaper, L., et al. 2003, A&A, 404, 249
Black, J. H., & Willner, S. P. 1984, ApJ, 279, 673
Brown, A. G. A., de Geus, E. J., & de Zeeuw, P. T. 1994, A&A, 289, 101
Cardelli, J. A., Clayton, G. C., Mathis, J. S. 1989, ApJ, 345, 245
Cesarsky, D. A. 1977, A&A, 54, 765
Chalabaev, A. A., & Léna, P. 1986, A&A, 168, L7
Chandler, C. J., Carlstrom, J. E., Scoville, N. Z., Dent, W. R. F., & Geballe, T. R. 1993, ApJ, 412, L71
Chandler, C. J., Carlstrom, J. E., Scoville, N. Z. 1995, ApJ, 446, 793
Clark, J. S., & Steele, I. A. 2000, A&AS, 141, 65
Codella, C., Felli, M., & Natale, V. 1994, A&A, 284, 233
Decin, L. 2000, Ph.D. Thesis, 16
Decin, L., Waelkens, C., Eriksson, K., et al. 2000, A&A, 364, 137
Frey, A., Lemke, D., Thum, C., & Fahrbach, U. 1979, A&A, 74, 133
Gaume, R. A., Johnston, K. J., & Wilson, T. L. 1992, ApJ, 388, 489
Geballe, T. R., Smith, H. A., & Fischer, J. 1987a, BAAS, 19, 728
Geballe, T. R., & Persson, S. E. 1987b, ApJ, 312, 297
Giannini, T., Nisini, B., Lorenzetti, D., et al. 2000, A&A, 358, 310
de Graauw, T., Haser, L. N., Beintema, D. A., et al. 1996, A&A, 315, L49
Grasdalen, G. L. 1974, ApJ, 193, 373
Hamann, F., & Simon, M. 1987, ApJ, 318, 356
Henning, Th., & Guertler, J. 1986, Ap&SS, 128, 199
Jiang, D. R., Perrier, C., & Léna, P. 1984, A&A, 135, 249
Kessler, M. F., Steinz, J. A., Anderegg, M. E., et al. 1996, A&A, 315, L27
Kruegel, E., Thum, C., Pankonin, V., & Martin-Pintado, J. 1982, A&AS, 48, 345
Kurtz, S., Churchwell, E., & Wood, D. O. S. 1994, ApJS, 91, 659
Kurucz, R.L. 1991, in Stellar atmospheres: beyond classical models, ed. L. Crivellari, I. Hubeny, & D. G. Hummer, NATO ASI Ser. C, 341, 441
Lenorzer, A., de Koter, A., & Waters, L. B. F. M. 2002a, A&A, 386, L5
Lenorzer, A., Vandenbussche, B., Morris, P., et al. 2002b, A&A, 384, 473
Maihara, T., Mizutani, K., & Suto, H. 1990, ApJ, 354, 549
Marlborough, J. M. 1969, ApJ, 156, 135
Mezger, P. G., Chini, R., Kreysa, E., Wink, J. E., & Salter, C. J. 1988, A&A, 191, 44
Millar, C. E., & Marlborough, J. M. 1998, ApJ, 494, 715
Millar, C. E., & Marlborough, J. M. 1999a, ApJ, 516, 276
Millar, C. E., & Marlborough, J. M. 1999b, ApJ, 516, 280
Millar, C. E., Sigut, T. A. A., & Marlborough, J. M. 2000, MNRAS, 312, 465
Mountain, C. M., Robertson, D. J., Lee, T. J., et al. 1990, SPIE, 1235, 25
Nisini, B., Smith, H. A., Fischer, J., & Geballe, T. R. 1994, A&A, 290, 463
Olnon, F. M. 1975, A&A, 39, 217
Panagia, N. 1973, AJ, 78, 929
Panagia, N., Felli, M. 1975, A&A, 39, 1
Plez, B., Brett, J. M., & Nordlund, A. 1992, A&A, 256, 551
Poeckert, R., & Marlborough, J. M. 1978, ApJ, 220, 940
Putman, M. E., Bjorkman, K. S., Wood, K., & Bjorkman, J. E. 1996, A&AS, 188, 5708
Ramesh, B., & Sridharan, T. K. 1997, MNRAS, 284, 1001
Simon, M., Felli, M., Cassar, L., Fischer, J., & Massi, M. 1983, ApJ, 266, 623
Smith, H. A., Fischer, J., Geballe, T. R., et al. 1984, in NASA Ames Research Center Airborne Astron. Symp., 164
Smith, L. J., Norris, R. P. F., & Crowther, P. 2002, MNRAS, 337, 1309
Snell, R. L., & Bally, J. 1986, ApJ, 303, 683
Teixeira, T. C., & Emerson, J. P. 1999, A&A, 351, 292
Thompson, R. I., Thronson, H. A. Jr., & Campbell, B.G. 1981, ApJ, 249, 622
Thronson, H. A., Lada, C. J., Schwartz, P. R., et al. 1984, ApJ, 280, 154
Vink, J. S., de Koter, A., & Lamers, H. J. G. L. M. 2001, A&A, 369, 574
Waters, L. B. F. M. 1986, A&A, 162, 121
Waters, L. B. F. M., Marlborough, J. M., van der Veen, W. E. C., Taylor, A. R., & Dougherty, S. M. 1991, A&A, 244, 120
Walsh, A. J., Burton, M. G., Hyland, A. R., & Robinson, G. 1998, MNRAS, 301, 640
Walsh, A. J., Bertoldi, F., Burton, M. G., & Nikola, T. 2001, MNRAS, 326, 36
Whittet, D. C. B., Bode, M. F., Longmore, A. J., et al. 1988, MNRAS, 233, 321
Wilson, T. L., Mehringer, D. M., & Dickel, H. R. 1995, A&A, 303, 840
Wood, D. O. S., & Churchwell, Ed. 1989, ApJ, 340, 265
Wright, A. E., & Barlow, M. H. 1975, MNRAS, 170, 41